Zitierweise: Angew. Chem. Int. Ed. 2024, e202412550
doi.org/10.1002/anie.202412550

VIP Batteries Very Important Paper

Interdependence of Support Wettability - Electrodeposition Rate-Sodium Metal Anode and SEI Microstructure

Chang-An Lo[+], Yixian Wang[+], Varun R. Kankanallu, Aditya Singla, Dean Yen, Xiaoyin Zheng, Kaustubh G. Naik, Bairav S. Vishnugopi, Callum Campbell, Vikalp Raj, Chonghang Zhao, Lu Ma, Jianming Bai, Feipeng Yang, Ruipeng Li, Mingyuan Ge, John Watt, Partha P. Mukherjee, David Mitlin, and Yu-chen Karen Chen-Wiegart**

Abstract: This study examines how current collector support chemistry (sodiophilic intermetallic Na_2Te vs. sodiophobic baseline Cu) and electrodeposition rate affect microstructure of sodium metal and its solid electrolyte interphase (SEI). Capacity and current (6 mAh cm^{-2}, 0.5–3 mA cm^{-2}) representative of commercially relevant mass loading in anode-free sodium metal battery (AF-SMBs) are analyzed. Synchrotron X-ray nanotomography and grazing-incidence wide-angle X-ray scattering (GIWAXS) are combined with cryogenic ion beam (cryo-FIB) microscopy. Highlighted are major differences in film morphology, internal porosity, and crystallographic preferred orientation e.g. (110) vs. (100) and (211) with support and deposition rate. Within the SEI, sodium fluoride (NaF) is more prevalent with Te–Cu versus sodium hydride (NaH) and sodium hydroxide (NaOH) with baseline Cu. Due to competitive grain growth the preferred orientation of sodium crystallites depends on film thickness. Mesoscale modeling delineates the role of SEI (ionic conductivity, morphology) on electrodeposit growth and onset of electrochemical instability.

[*] C.-A. Lo,[+] V. R. Kankanallu, D. Yen, X. Zheng, C. Zhao, Y.-c. Karen Chen-Wiegart
Department of Materials Science and Chemical Engineering, Stony Brook University, Stony Brook, NY, 11794, USA
E-mail: Karen.Chen-Wiegart@stonybrook.edu

Y. Wang,[+] C. Campbell, V. Raj, D. Mitlin
Materials Science and Engineering Program & Texas Materials Institute, The University of Texas at Austin, Austin, TX, 78712 USA
E-mail: david.mitlin2@utexas.edu

A. Singla, K. G. Naik, B. S. Vishnugopi, P. P. Mukherjee
School of Mechanical Engineering, Purdue University, West Lafayette, IN 47907, USA

L. Ma, J. Bai, F. Yang, R. Li, M. Ge, Y.-c. Karen Chen-Wiegart
National Synchrotron Light Source II, Brookhaven National Laboratory, Upton, NY, 11973, USA

J. Watt
Center for Integrated Nanotechnologies, Los Alamos National Laboratory, Los Alamos, NM 87545, USA

[+] These authors contributed equally to this work.

Introduction

Sodium ion batteries (SIBs) and sodium metal batteries (SMBs) are promising options in next-generation energy storage technology.[1] However, before sodium metal can be rightfully considered as a viable anode it has to overcome the critical challenge of interfacial instability during electrodeposition/dissolution.[2] For anode-free SMBs (AF-SMBs), where the cathode is the only ion reservoir, the challenge is to achieve stable electrodeposition/dissolution onto an "empty" current collector, rather than onto pre-existing sodium metal.[3] Employing tailored support structures is one established approach to enhance the electrochemical stability of sodium metal.[4] Other approaches to stabilize the SEI and to prevent dendrites include various additives,[5] artificial SEI structures with purposely introduced inorganic phases,[6] and macroscopically three dimensional current collectors with tuned sodiophilicity.[7]

An established methodology for enhancing the electrochemical stability of metal anodes is to employ current collector underlayers that alloy with the alkaline metal at every cycle, homogenizing electrodeposition/dissolution, and in effect serving as miniature reversible ion anodes.[8] The associated reversible alloying reactions have been examined by the sodium ion-battery anode community and involve major volume changes, in some cases on the order of 300 %. In this study we employ a model system based on a sodiophilic composite of Na_2Te intermetallics and Cu microparticles. The key rationale for using this composite support is that it "does not move", i.e. there are no volume changes during electrodeposition/dissolution of Na. Both Na_2Te and Cu are thermodynamically stable at anode-relevant voltages. During cycling such supports do not react with Na, and yet remain highly sodiophilic due to the nature of the electronic structure of the alkaline-ion containing intermetallic.[9]

A range of techniques have been employed to characterize sodium metal and SEI, including cryogenic electron microscopy (Cryo-EM),[10] X-ray photoelectron spectroscopy,[11] nuclear magnetic resonance,[12] synchrotron-based X-ray powder diffraction,[13] pair distribution function analysis,[13] and laser scanning confocal microscope.[14] More generally, while synchrotron X-ray-based methods have been applied to Li metal batteries,[15] work on SMBs is more scarce.[16] Authors have also studied the site-specific crystallography of Na metal using Cryo-EM.[10d] Despite these

significant advances, the heterogeneous nature of the reactive growing/shrinking metal - electrolyte interphase remains not fully understood. With SMBs and AF-SMBs the preferred crystallographic orientation of the metal and of the SEI components remains largely unexplored. How these two potentially important microstructural features related to the chemistry of the underlying current collector, and how they relate to the electrodeposition rate, are also unknown. Here we present a first of its kind multimodal investigation of the interdependence of the current collector support sodiophilicity/phobicity, electrodeposition current density, and sodium metal and associated SEI structure (morphology, porosity, preferred orientation).

Results and Discussion

To investigate the influence of the surface chemistry of a current collector on Na electrodeposition, experiments were carried out using Cu_2Te-coated Cu foil (termed "Te–Cu") as the model system,[17] with commercial Cu foil as a baseline (termed "Cu"). Details of the synthesis process, the resultant structure of Te–Cu, and additional refences are provided in the Supporting Information.

Electrochemical measurements were conducted using a two-electrode half-cell configuration in coin cells, representing an AF-SMB configuration. A rolled Na metal foil served as the counter and reference electrode. An ether-based electrolyte consisting of 1 M $NaPF_6$ in diglyme (G2) was employed, having been shown to promote more stable electrodeposition and electrodissolution compared to carbonate-based electrolytes.[18] Prior to testing, all cells were subjected to an activation process, involving cycling within a voltage window of 0–1 V for five cycles at 0.1 mA cm^{-2}. During this activation step an irreversible conversion reaction occurs that transforms the Cu_2Te intermetallics into a composite layer of Na_2Te (*fcc* anti-fluoride structure) and Cu microparticles. In-depth analysis of the process is detailed in reference.[3b] The sodiophilic Na_2Te is thermodynamically stable at anode-relevant voltages, while the Cu microparticles allow for the coated current collectors to remain electrically conductive. Additional four activation cycles were subsequently performed to ensure a robust SEI layer on the collector surfaces. A voltage of 0 V vs. Na/Na$^+$ is above that necessary for electrodeposition of Na, so the actual electrodeposition experiments were started with an "empty" current collector.

The surface morphology of the Te–Cu and Cu supports was characterized using scanning electron microscopy (SEM) and optical profilometry. Figures S1(a) and S1(b) show SEM images of the initial Cu_2Te layer formed on the Te–Cu support and of the baseline Cu, respectively. It may be observed that the Cu_2Te crystallites are on the scale of one to several micrometers, being densely and uniformly distributed on the Cu surface. To quantify the associated surface roughness, analysis was performed using optical profilometry. Figures S1(c) and S1(d) present the 3D topographic maps of Te–Cu and Cu. The average roughness (S_a) for Te–Cu is 0.283 ± 0.379 μm with a maximum roughness (S_z) of 4.740 μm. In comparison, the baseline Cu has an S_a of 0.248 ± 0.297 μm and an S_z of 2.222 μm. This indicates a slight increase in the surface roughness due to the Cu_2Te coating. Detailed crystallographic information will be examined using synchrotron-based techniques, which will be discussed later in the manuscript.

Figures 1(a) and 1(b) display the galvanostatic profiles of Na half-cells utilizing Te–Cu and Cu as the current collector. The Te–Cu half-cell exhibits a prolonged plateau at ~1.1 V. This plateau is primarily associated with the irreversible conversion reaction $Cu_2Te + 2Na^+ + 2e^- => Na_2Te + 2Cu$, with irreversible SEI formation also contributing. It may be observed that this conversion reaction is not reversed during subsequent desodiation, or in the next four cycles. The irreversible reduction plateau for the baseline Cu is significantly shorter, being associated only with SEI formation. It has been reported that underpotential metal deposition can occur due to the strong adatom/substrate bonding, contributing to the reversible capacity of a material, especially if the substrate surface area is large.[19] If present, such capacity would be highly reversible, with adsorption/dissolution of adatoms requiring vanishingly small overpotentials. To further exclude the possibility of underpotential deposition of Na on the two supports, cyclic voltammetry (CV) measurements were performed using a three-electrode configuration. A relatively slow scan rate of 0.1 mV s^{-1} was employed. As shown in Figure S2, for Te–Cu the major reduction peak is centered near 1 V. During the subsequent anodic scan, no oxidation peak is present. For baseline Cu, the reduction peak centered near 0.6 V is associated SEI formation only. Neither specimen manifests significant redox peaks in the subsequent cycles. Such electrochemical signatures rule out underpotential deposition of Na as a contributor to the reversible capacity for either support. Figures S3 and S4 show the XRD profiles of the two collectors after this cycling regiment. As expected, there is no evidence of Bragg peaks associated with crystalline Na metal.

Following the activation process, rate-dependent Na electrodeposition was performed, with the associated voltage profiles being provided in Figures 1(c) and 1(d). Three current densities (0.5, 1, and 3 mA cm^{-2}) were selected with a fixed Na electrodeposition capacity of 6 mAh cm^{-2}, corresponding to a deposited Na thickness of 54 μm. This is significantly more aggressive current-capacity regiment as compared to typical scientific literature (e.g. 0.5 mA cm^{-2} and 0.5 mAh cm^{-2}), aiming to be representative for industrially relevant high mass loading cathode in an AF-SMB configuration. The nucleation overpotentials of Na on Te–Cu substrate are 20, 36, and 85 mV at 0.5, 1, and 3 mA cm^{-2}, respectively. The corresponding values for the baseline Cu collector are 96, 116, and 158 mV. These results demonstrate a reduced barrier for Na nucleation on the Te–Cu surface as compared to Cu. In addition to the improvement of Na nucleation, the sodiophilic Na_2Te coating also contributes to enhanced cycling performance at different current densities. Figures 1(e) and 1(f) show that at a current of 1 mA cm^{-2}, the Te–Cu half-cell can stably cycle for more than 350 cycles, while the baseline Cu hall-cell fails

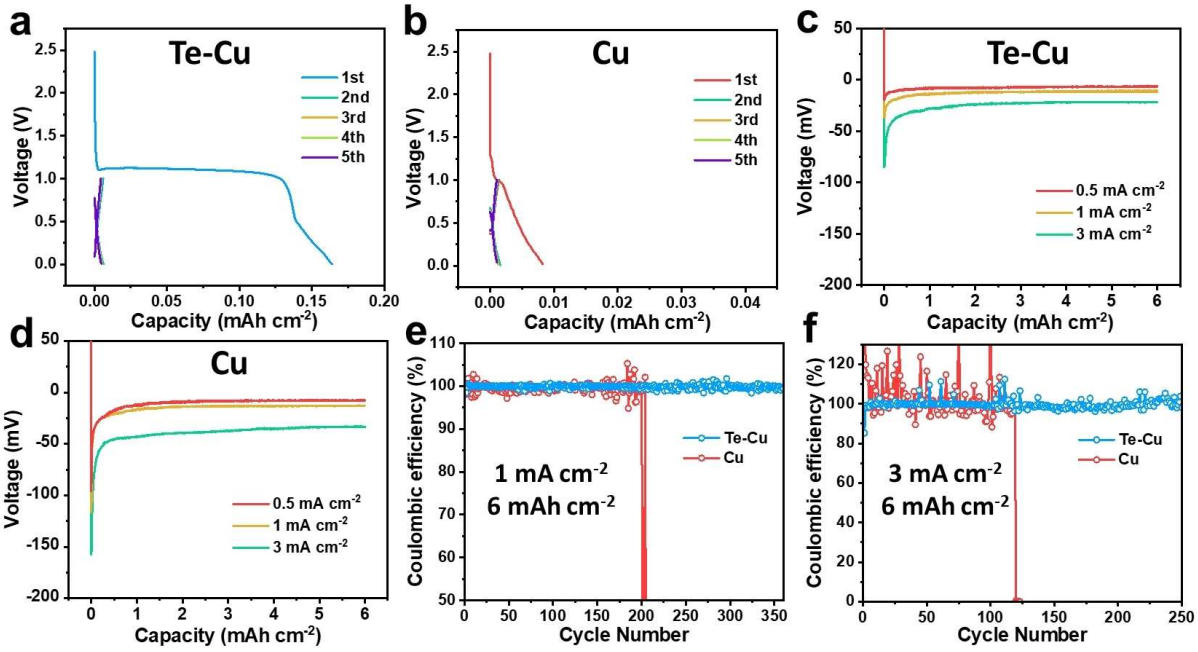

Figure 1. (a–b) Galvanostatic cycling profiles for Te–Cu and baseline Cu during activation cycles, tested at 0.1 mA cm^{-2}. (c–d) Galvanostatic electrodeposition profiles for Te–Cu and baseline Cu, respectively. Testing performed at current density of 0.5, 1 or 3 mA cm^{-2}, to a fixed capacity of 6 mAh cm^{-2}. (e–f) Cycling performance for Te–Cu and baseline Cu at 1 mA cm^{-2} or 3 mA cm^{-2}, to a fixed capacity of 6 mAh cm^{-2}.

around 200 cycles. A similar trend is observed at a higher current of 3 mA cm^{-2}, where the Te–Cu half-cell achieves more than 250 cycles, while the baseline Cu cell shows fluctuating cycling Coulombic efficiency (CE) starting from the onset.

As a proof-of-concept, AF-SMB full cells employing $Na_3V_2(PO_4)_3$ (NVP) cathodes with Te–Cu and baseline Cu current collectors were assembled and tested. Employed was a voltage window of 2.8–3.8 V, and a current density of 1 C (1 C = 118 mAh g^{-1}, based on the mass of NVP cathode). As shown in Figure S5, the initial charge/discharge capacities are 122/97 mAh g^{-1} and 117/81 mAh g^{-1} for Te–Cu and Cu cells, respectively. This corresponds to an initial Coulombic efficiency (ICE) of 79 % and 69 %, respectively. The Te–Cu AF full cell exhibits discharge capacities of 94, 92, 86, and 81 from cycle 2 to cycle 5, with an average cycling CE of 93 % over the first 20 cycles. By contrast, the baseline Cu AF full cell rapidly degrades, with cycle 2 to cycle 5 discharge capacities being 81, 51, 28, and 4 mAh g^{-1}. As achieving state-of-the-art performance is not the focus of this paper, the subsequent analysis will mainly concentrate on the initial Na electrodeposition process at different current densities.

Figure 2 and Figures S6–S10 compares cross-sectional cryogenic focused ion beam (Cryo-FIB) SEM and associated energy-dispersive X-ray spectroscopy (EDXS) maps for Na electrodeposited on Te–Cu and baseline Cu. Per the EDXS maps, it may be observed that the composite Na_2Te–Cu microparticle layer remains adherent to the underlying collector, with electrodeposition occurring on its surface. With the Te–Cu collector the Na films are dense, largely free from pores, and display a uniform surface morphology. With a current of 0.5 mA cm^{-2}, the thickness of the deposited Na film on Te–Cu was 58 μm, close to the theoretical value of 54 μm (1 mAh cm^{-2} = 9 μm). Conversely, for the baseline Cu, the accumulated Na film measures 69 μm, the discrepancy being attributable to a combination of micro-scale internal porosity in the film and meso-scale non-uniformity in its morphology. Per the EDXS O and F maps for baseline Cu, there are spherical SEI inclusions present in the bulk of the electrodeposit. These likely originate from open pores that during deposition were in contact with the electrolyte. At 1 mA cm^{-2}, the electrodeposit on Te–Cu remains dense and morphologically uniform. The thickness of the Na film is calculated to be 55 μm, closely aligning with the theoretical value. In contrast, the 1 mA cm^{-2} electrodeposit on baseline Cu is morphologically uneven. In the region analyzed, the film thickness is 48 μm. At current of 3 mA cm^{-2}, the Na deposited on Te–Cu is still generally dense and uniform in its morphology, with an overall thickness of 55 μm. The thickness of the Na deposited on baseline Cu is 77 μm. The findings from the cryo-FIB-SEM analysis substantiate the general conclusion that metal electrodeposition on "phobic" supports is non-uniform due to poor wetting.

To preserve the electrodes for studying the nature of solid electrolyte interphase (SEI) formation and morphological changes, a series of precautions were taken: The coin cells were disassembled in an argon-filled glovebox right before conducting the measurements. The Na electrodeposits on the supports were not washed by solvent, which could induce changes to the SEI structure. Instead, the samples were directly mounted on holders and subjected to evacuation overnight to remove any residual electrolyte. Prior to measurement, the samples were sealed within a mobile

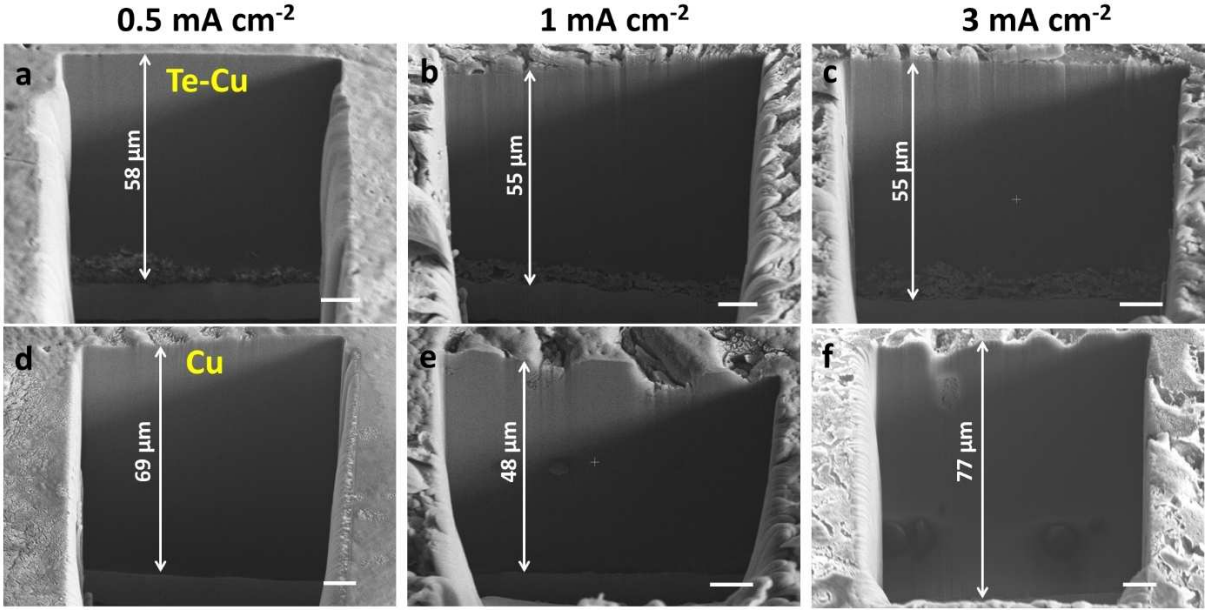

Figure 2. (a–c) Cryo-FIB-SEM cross-sectional images of Na electrodeposited on Te–Cu to a fixed capacity of 6 mAh cm^{-2} . (d–f) Same analysis for baseline Cu. Current densities employed: (a, d) 0.5 mA cm^{-2}, (b, e) 1 mA cm^{-2}, and (c, f) 3 mA cm^{-2}. The scale bar is 10 µm.

chamber, which was subsequently mounted on the end-station of the synchrotron beamline for the experiment. It should also be noted that efforts are underway to develop synchrotron operando methods that enable analysis of the electrodes without the disassembly step. However this approach remains challenging due to the experimental geometry, and is not yet ready to be utilized for collecting repeatable data. Once successful, such an approach will provide kinetic information about the metal electrodeposition at operando conditions, complementing the post-mortem results.

Transmission X-ray Microscopy (TXM) analysis was performed on the FXI beamline of NSLS-II,[20] with details provided in the Supporting Information and in Figure S11. Figures 3 and 4 show the nano-tomography analysis of electrodeposited Na on baseline Cu support and on the Te–Cu support, respectively. Figure 3**(a)** provides a schematic representing the TXM setup. Figure 3**(b)** shows a 3D visualization of electrodeposited Na on baseline Cu, with the videos available in the Supporting Information (Movie S1–S3). Despite a fixed areal capacity corresponding to theoretical 54 µm, the actual film thickness progressively increases with current density. At 0.5 mA cm^{-2} the Na electrodeposit is measured to be approximately 75.5 µm thick, at 1 mA cm^{-2} it is 84.7 µm thick, and at 3 mA cm^{-2} it is 85.9 µm thick. It may be observed that electrodeposits on the baseline Cu collector are not fully dense and that the electrodeposit is morphologically heterogeneous. Per the macro photographs presented Figure S12, there are significant site-to-site thickness variations for the Na electrodeposit thickness on the baseline Cu.

Figure S13 provides schematics of X-ray scattering, performed in transmission and reflection geometries, respectively. Figures S14 - S15 provide details of analysis in reflection geometry, with the associated discussion being in the Supporting as well. Before proceeding to describe Na metal and its SEI, the grazing-incidence wide-angle X-ray scattering (GIWAXS) results for the as-synthesized current collectors are presented. Figures S16 presents the 1D GIWAXS patterns and associated analysis for the Te–Cu and Cu collectors in their as-fabricated state (no electrochemical testing). The ratio between the peaks and its deviation from randomly orientated crystallites (labeled "PDF" on bar charts) would indicate the presence of preferred orientation in the film. Figures S16(a)–S16(b) provide the indexed GIWAXS patterns for baseline Cu and Te–Cu supports, respectively. Figure S16(c) shows analysis for the relative peak intensities for the baseline Cu support, indicating that the crystallites near the foil surface primarily possess a (200) preferred orientation, with (111) orientation being the minority. Figure S16(d) provides the relative peak intensities for the underlying unreacted Cu foil in the Te–Cu support. It may be observed that in this case the preferred orientation of the Cu crystallites is primarily (111), with some (200). This change in orientation may be explained by the thermal evaporation process (foil and Te source both held at 600 °C for an hour in an argon atmosphere), which caused Cu recrystallization and grain growth. Both (200) and (111) preferred orientations agree with the well-known textures of electrodeposited or rolled Cu foils. Figure S16(e) shows the relative peak intensities for the Cu_2Te layer. The *hexagonal* (P6/mmm) Cu_2Te crystallites display a combination of (100), (101) and (103) preferred orientations. It should be again pointed out again that the Cu_2Te phase does not exist after the first sodiation to 0 V, being transformed to a composite of Na_2Te and Cu microparticles.

Figure S17 presents the XRD patterns measured in transmission geometry for Na metal with Cu and with

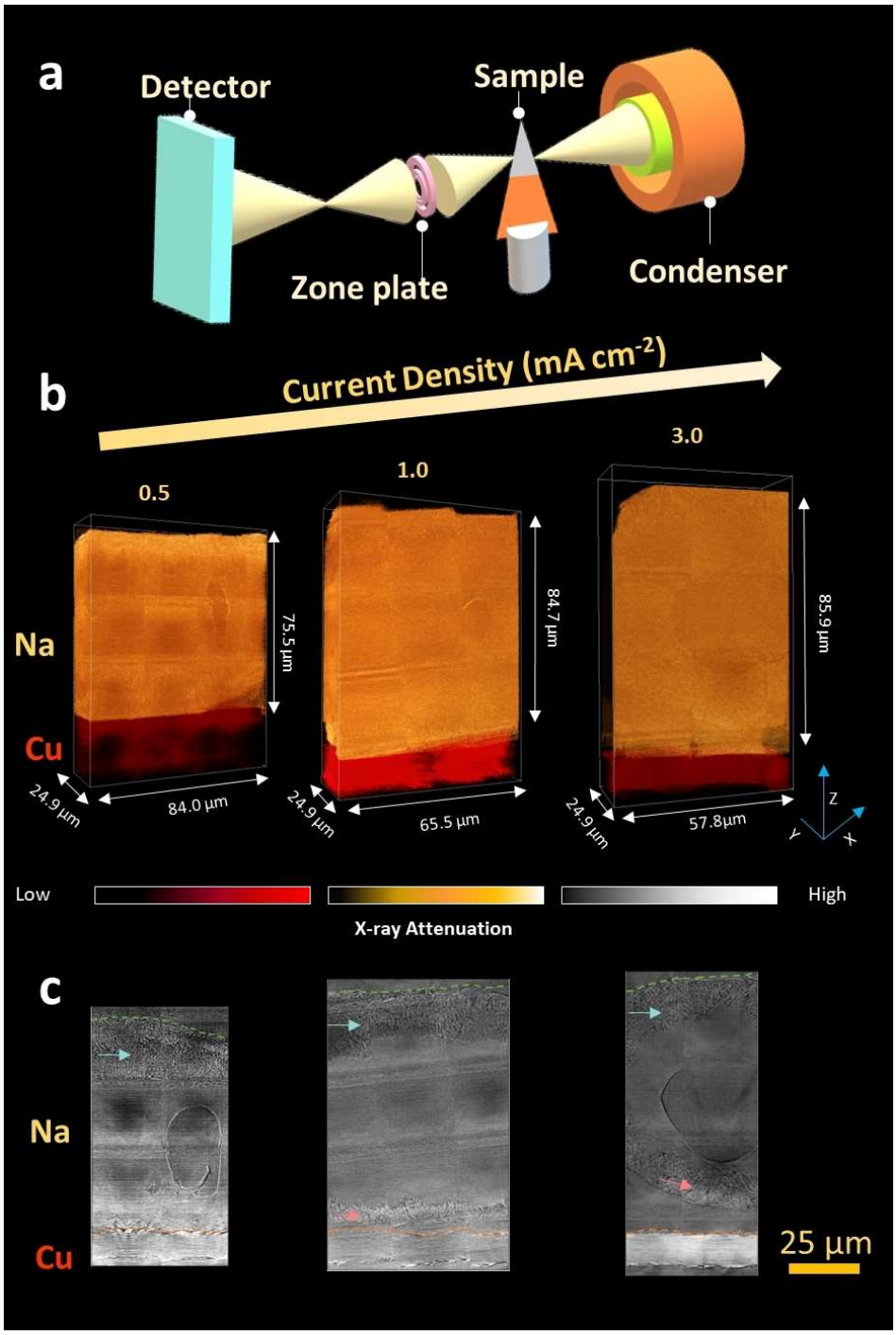

Figure 3. 3D synchrotron X-ray nano-tomography by transmission X-ray microscopy (TXM) for visualizing the internal structure of the deposited Na on Cu as a function of current density, from 0.5, 1.0 to 3.0 mA cm^{-2} with a constant capacity of 6 mAh cm^{-2}. (a) A schematic representing the TXM optics layout at the FXI beamline, NSLS-II. (b) 3D tomographic volume rendering and (c) their corresponding pseudo cross-sectional 2D images along the XZ plane and the cyan and pink arrows indicate surface and interface Na structures, respectively.

Te–Cu supports, analyzed at various current densities. Peaks corresponding to three sets of Na planes are identified: (110), (200), and (211). Minimal crystalline SEI phases are detected, indicating that the transmission mode is not well-suited for SEI analysis. Employing reflection geometry, however, it is possible to analyze both the Na metal and it′s crystalline SEI components. Therefore analysis was performed in reflection geometry, with an in-depth schematic of the methodology being provided in Figure 5(a). Figures 5-(b) and 5(c) show the integrated and averaged 1D GIWAXS patterns of electrodeposited Na on baseline Cu and on Te–Cu for 0.5 mA cm^{-2}. Figure S18 displays this analysis for

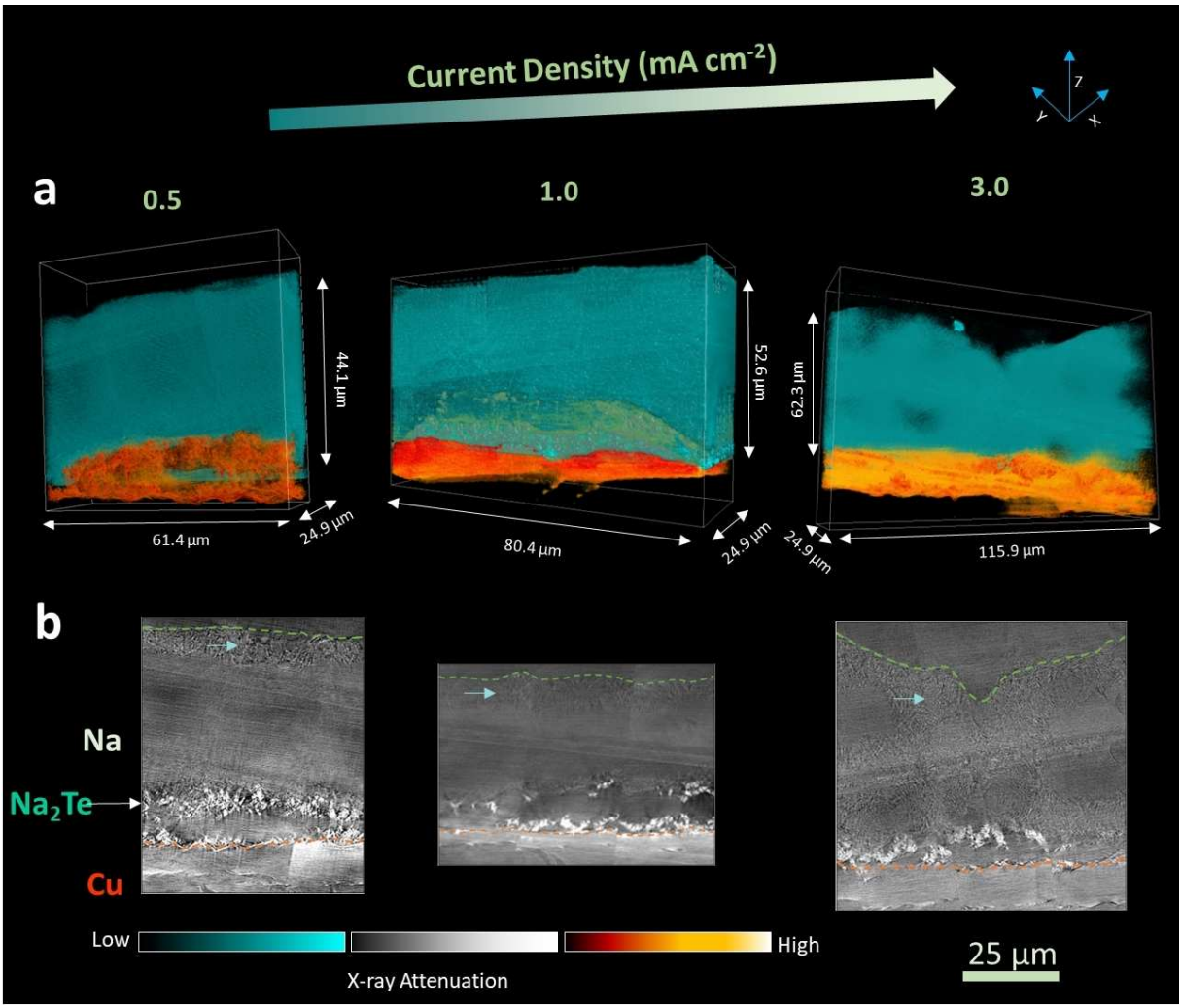

Figure 4. 3D synchrotron X-ray nano-tomography by transmission X-ray microscopy for visualizing the internal structure of the deposited Na on Te–Cu as a function of current density, from 0.5, 1.0 to 3.0 mA cm^{-2} with a constant capacity of 6 mAh cm^{-2}. (a) 3D tomographic volume rendering and (b) Corresponding pseudo cross-sectional 2D images along the XZ plane. Cyan arrows indicate surface Na structures.

1 and 3 mA cm^{-2} current densities. Figures 5(d)–5(f) provide the orientation intensity distribution bar graphs for Na metal with baseline Cu at 0.5, 1 and 3 mA cm^{-2}, comparing the distribution to what is expected for random grain orientation. Figures 5(g)–5(i) provide the same analysis for Na metal with Te–Cu supports. The bar charts show scaled Na diffraction peak areas for Na (110), Na (200) and Na (211) vs. incident X-ray beam angle, corresponding to different probing depths. The ratio between the peaks and its deviation from randomly orientated crystallites would indicate the presence of preferred orientation in the film. From the results it may be observed that the Na preferred orientation varies with the film thickness and has a complex rate and support dependence. Considering the baseline Cu support first, it may be observed that at 0.5 and 1 mA cm^{-2} the preferred orientation of the Na electrodeposit depends on which portion of the film is being probed by the X-rays, i.e. directly near its surface versus 21 µm into the film thickness.

For Na metal deposited on baseline Cu supports at 0.5 and 1 mA cm^{-2}, the film preferred orientation is a combination of (100) and (110). Since it was not possible to generate complete pole figures for these specimens, one cannot provide a full description of the crystallographic texture. However, likely all the metal films possess a fiber texture, i.e. individual Na crystallites with (100) or (110) being parallel to the collector surface and arbitrarily rotated around the surface normal. For the Te–Cu support, a sharper (110) preferred orientation is observed at all deposition rates and probing depths. Per the measured overpotentials, Na crystallite nucleation is easier on the sodiophilic Te–Cu than on the sodiophobic baseline Cu. At 3 mA cm^{-2}, both Cu and Te–Cu supports yield an equally strong, almost entirely dominant, (110) orientation. This indicates that a (110) preferred orientation is associated with a lower nucleation barrier (lower overpotential) and with greater nucleation rate due to the higher current density.

It is instructive to first consider the early-stages of film growth, when the electrodepositing Na metal is coming into

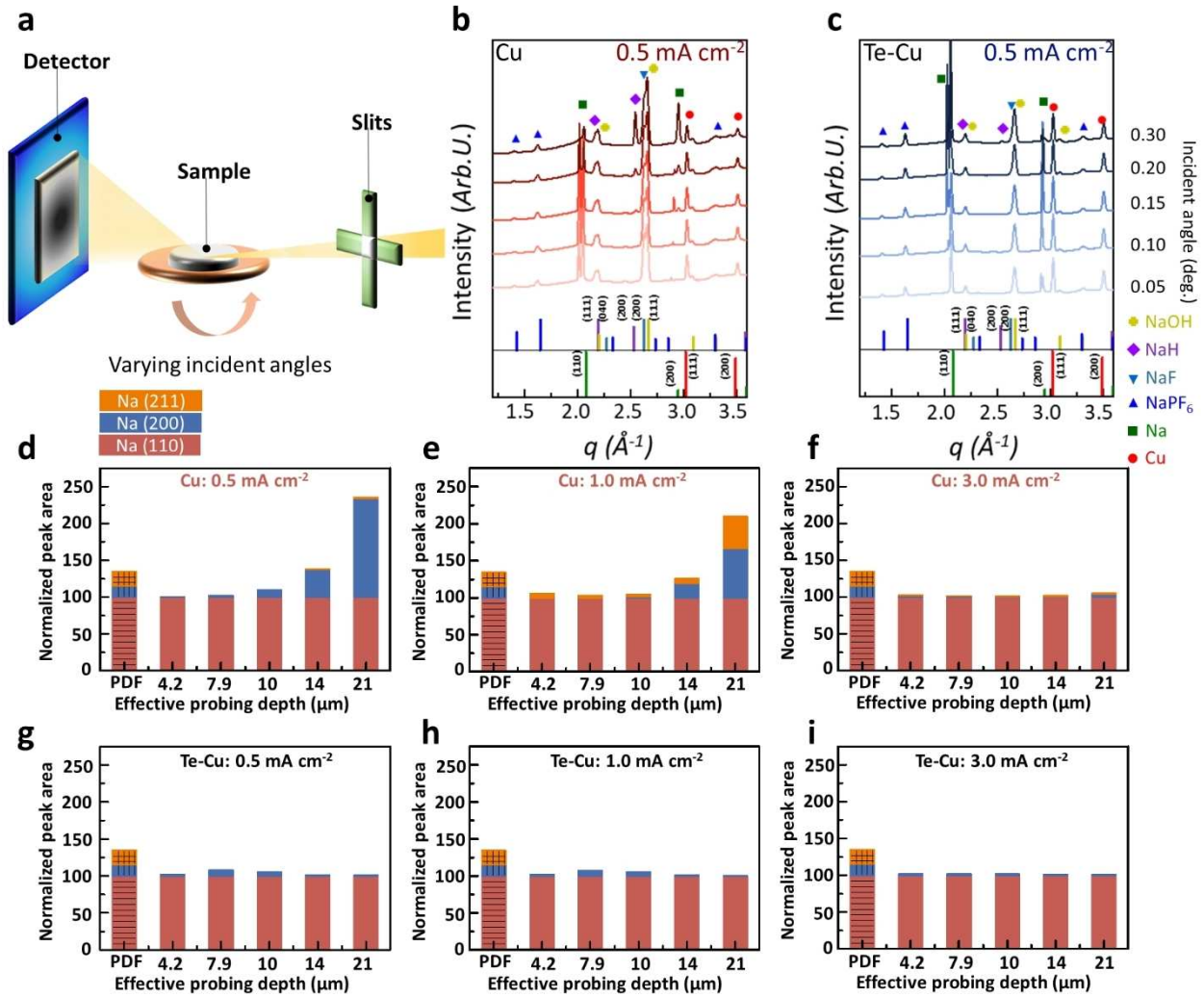

Figure 5. Depth-dependent preferred orientation analysis for deposited Na metal. (a) Schematic of the GIWAXS setup. (b) and (c) Representative indexed GIWAXS patterns for 6 mAh/cm^2 of Na on baseline Cu and Te–Cu, deposition performed at 0.5 mA cm^{-2} (PDF#00–001–0850). Additional indexed patterns are shown in the Supporting Information. (d–f) Orientation intensity distribution bar graphs for baseline Cu at 0.5, 1 and 3 mA cm^{-2}, comparing with what is expected for random grain orientation. (g–i) Same analysis for Te–Cu supports. The bar charts show scaled Na diffraction peak areas for Na (110), Na (200) and Na (211) intensity vs. incident X-ray beam angle, corresponding to different probing depths.

contact with Na_2Te+Cu microparticles or with the bare Cu foil. Since the collectors were first electrochemically conditioned prior to electrodeposition, it is expected that the SEI covered collector surfaces would be free of native copper oxide. Therefore it is reasonable to assume that the incoming Na would largely see a metallic or an intermetallic surface. The preferred orientation of Na crystallites on a heterogeneous support depends on a balance of interface strain energy and interface chemical energy. With the Te–Cu supports, the lower overpotentials versus baseline Cu signal easier initial-stage Na nucleation on that surface.

Several *bcc* (Na) - *fcc* (Cu or Na_2Te) orientation relationships (OR′s) are known to exist between individual *bcc* and *fcc* crystallites (precipitates in a matrix, bilayer films, *etc.*). These include the well-known Kurdjumov-Sachs OR {110}*bcc*//{111}*fcc*, and <111>*bcc*//<110>*fcc*, Nishiyama-Wasserman OR {110}*bcc*//{111}*fcc.* and <100>*bcc*//<110>*fcc.* The Invariant Line OR, where the common direction corresponds to the vector of least distortion and is intermediate between <111> and <100>, has also been reported.[21] Such orientation relationships are generally driven by strain energy considerations, even if there is no direct epitaxial relationship between the support and the electrodeposit. Chemical interfacial energy considerations have also been shown to favor analogous ORs for individual crystallites comprising a *bcc* - *fcc* interface.[22] Polycrystalline metallic sheets or polycrystalline thin films often possess a fiber texture, i.e. crystallites having one or several sets of low-index planes parallel to the surface, but randomly rotated around the surface normal. One would expect this to be the case with the Na films and with the underlying Cu support. This does not preclude the presence of well-defined OR′s between the *individual* crystals of *bcc* Na metal and *fcc* Cu or *fcc* Na_2Te. Rather it indicates that collectively, the preferred orientation is based on {110}//{111}. It should be noted that more extensive analysis is required to construct

the pole figures necessary to properly determine the crystallographic texture of the Na films and of their underlying supports.

After the initial Na crystalline layer is deposited on the Te–Cu or Cu supports, the subsequent electrodeposit will only "see" Na metal (the Te–Cu or Cu becomes covered over). The case then becomes of Na nucleation on a homogeneous support, i.e. on pre-existing Na metal. During electrodeposition, there will be additional Na crystal-on-Na crystal nucleation, and as well as grain growth. The growth velocities of the individual Na crystallites will depend on their crystallographic orientation relative to the incoming ion flux. It has been reported that the activation energy for Li adatom diffusion on the Li (110) is about half the value it is for Li (100), being 0.046 eV and 0.09 eV, respectively. At room temperature this results in significantly faster growth rate of a Li (110) terminating crystallite surface.[23] While to our knowledge, these values have not been calculated for Na (110) versus Na (100), the overall conclusion should be analogous: Sodium adatoms will diffuse faster on the closer packed (110) relative to other crystalline facets. As the electrodeposited capacity increases and the film thickens, the faster growing - preferably oriented grains will subsume the slower growing less preferably oriented ones. The Na crystallites with one [110] direction normal to the foil surface will grow faster than the ones with the [100] direction normal to the surface. The slower growing (100) terminating grains will therefore become subsumed by the faster growing (110) grains.

Such an evolutionary growth mechanism causes the film texture to progressively sharpen with increasing film thickness. Also known as *Van der* Drift film growth, it has been detailed in literature both experimentally and through modeling.[24] *Van der* Drift growth modality is widely observed for deposited polycrystalline metals, semiconductors and oxide films.[25] For a range of electrochemically and vapor deposited materials, the sharpening of texture is known to be accelerated with increasing deposition rates. With both supports, (110) preferred orientation is the strongest at the highest current density, i.e. 3 $mA\,cm^{-2}$. This is attributed to the known effect of increasing electrodeposition rates in promoting more copious nucleation, in-turn due to a higher driving force and less time for diffusion to occur.[26] Prior studies on Li metal electrodeposition indicate that film preferred orientation is related to electrochemical stability.[23a,27] In the current study, Na films electrodeposited on Cu–Te cycles substantially better than films identically deposited on the baseline Cu. This provides a *correlation* between (110) preferred orientation and improved electrochemical stability, especially at low and intermediate currents. Establishing a direct *causal* relationship between the two would require further and more in-depth analysis, however.

Sputter-down X-ray photoelectron spectroscopy (XPS) was employed to investigate the differences in the Na metal SEI with Te–Cu versus with baseline Cu supports. These results are presented in Figures S19–S20, Tables S1–S2, and are discussed in detail within the Supporting Information. Analyzed were the 0.5 $mA\,cm^{-2}$ and the 3 $mA\,cm^{-2}$ to 6 $mAh\,cm^{-2}$ specimens. In summary, the key differences in Na electrodeposition between Te–Cu and baseline Cu lie in the initial SEI thickness and compositions. The SEI on the Te–Cu substrate is thinner and rich in sodium fluoride (NaF) and sodium phosphate ($NaPO_x$), whereas the SEI on baseline Cu is thicker and dominated by sodium fluorophosphate such as Na-PF_x and Na-PF_xO_y. The SEI layer on Na metal is known be a composite of inorganic and organic phases, some inorganic phases being crystalline[2829] A uniform distribution of NaF within the SEI is known to promote electrochemical stability.[29b,30] With Te–Cu, the Na metal SEI is richer in NaF and is more electrochemically stable, agreeing with these general findings.

GIWAXS was employed to further analyze the crystalline NaF, NaOH and NaH phases within the SEI. Those results are shown in Figure 6. It may also be observed that at higher deposition rates there is relatively less NaH/NaOH versus NaF. This is a clear trend with both support types. The relative amount of NaH and NaOH is especially elevated for baseline Cu at 0.5 $mA\,cm^{-2}$. It may be observed that the preferred orientation of the NaH and NaOH has a rate dependence to it as well. It is possible to calculate the standard enthalpies for NaOH and NaH formation using the Materials Project database.[31] The NaOH phase is likely result from exposure of Na_2O to residual to H_2O in the electrolyte, for the following reaction sequence: $Na_2O + H_2O => 2NaOH$, ΔH^0=-55.5 kJ/mol. The NaH can form from the H_2 gas that evolved from other decomposition reactions that comes in contact with Na metal: $Na + 0.5H_2 => NaH$, ΔH^0=-56.5 kJ/mol. For lithium metal batteries, LiH has been discussed as a potentially important SEI component,[32] and some recent work in sodium metal batteries also started to identify NaH phases in the SEIs.[33]

The depth-dependent preferred orientation of NaH is shown in Figure S21, with an extensive discussion being provided in the Supporting. With both supports the NaH is primarily present on the roughened surface of the metal electrodeposits. Moreover, with baseline Cu there is some NaH imbedded in the pores as well. It may be observed that preferred orientation of NaH differs between Te–Cu and baseline Cu. With baseline Cu, preferred orientation also dependents on the electrodeposition rate and the probing depth. This is indicative of the overall heterogeneous microstructure of the Na electrodeposits on this sodiophobic surface: It is in effect a composite of (majority) Na metal intermixed with (minority) pores, electrochemically formed SEI, NaH and NaOH. Authors have argued that since LiH is a wide gap insulator it is deleterious to electrochemical performance, causing electrical isolation and a loss of active ion inventory.[32a] Since NaH leads to electrical isolation of Na metal, its formation is deleterious. Clear trends are observed when considering the relative fraction of NaH and NaOH versus NaF. With Te–Cu, the SEI contains markedly less NaH and NaOH and more NaF. One can hypothesize that a continuous layer for NaF will block the reaction of the underlying Na metal with H_2 and H_2O. This would explain this trend and provide a direct link between the current collector support energetics and the Na metal SEI structure.

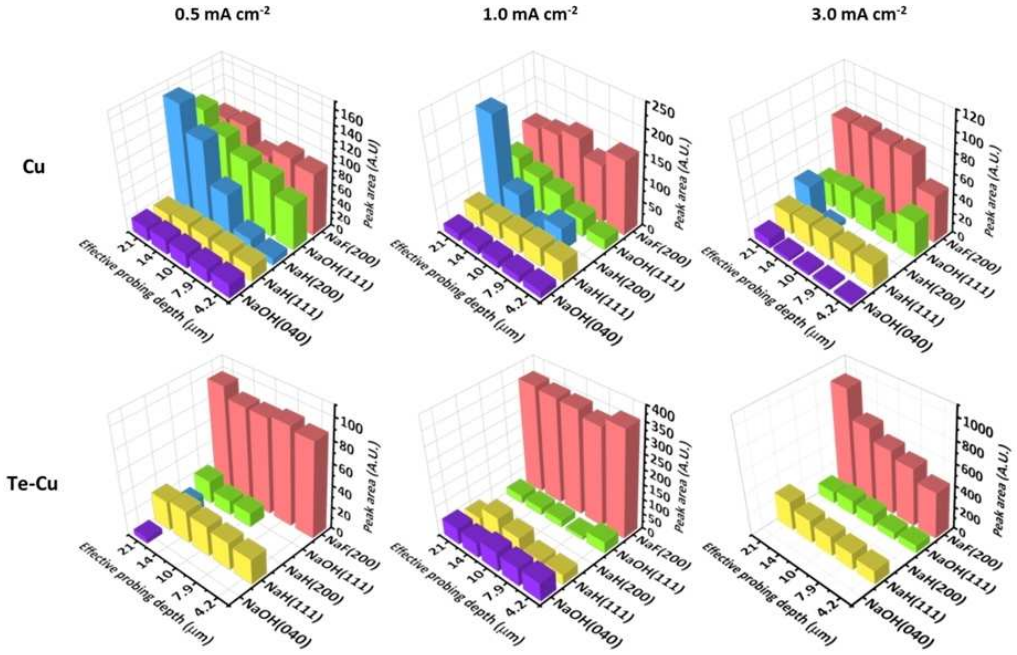

Figure 6. Depth-dependent preferred orientation analysis for the crystalline SEI components NaF, NaOH and NaH. Same specimens and technique as presented in Figure 5.

A mesoscale model was developed to delineate the role of SEI on Na deposition behavior. Figure 7(a) shows the difference in SEI structure for substrates with different surface energies. A substrate with high surface energy (Te–Cu electrode) will ensure proper SEI wetting and form a more uniform SEI compared to a substrate with low surface energy (Cu electrode). The SEI morphology is quantified using the descriptor, h/t, where h is the difference

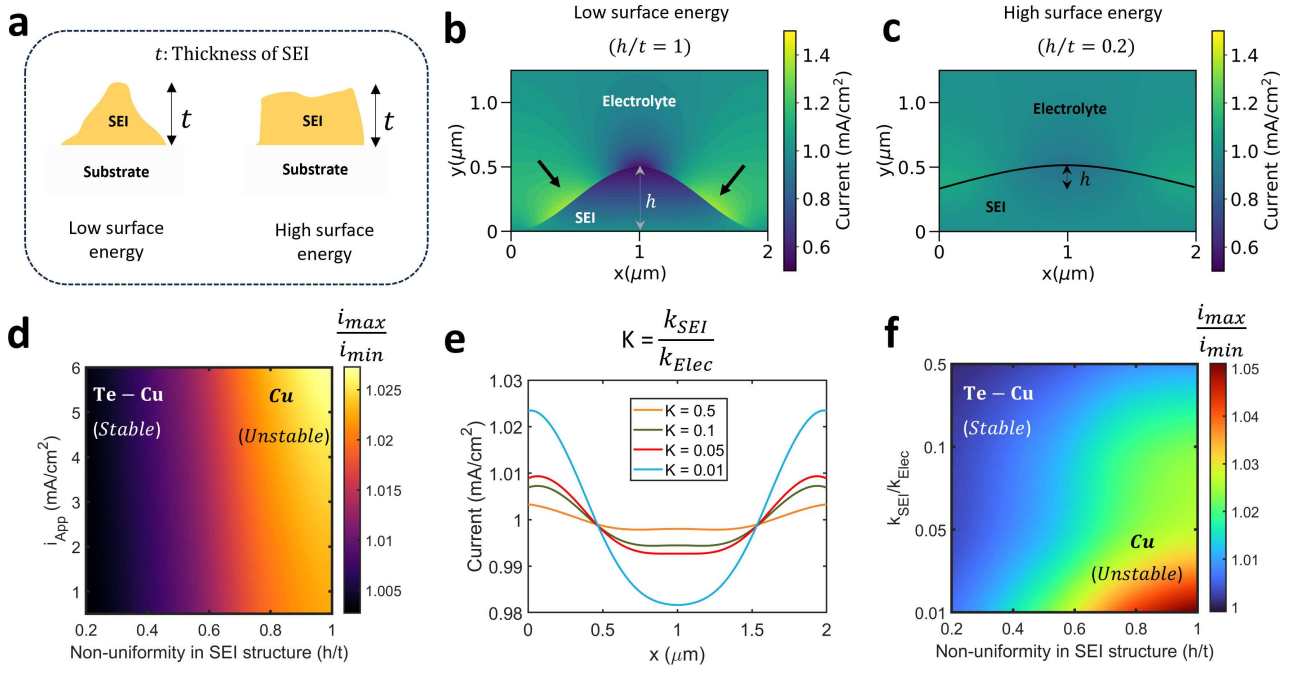

Figure 7. Electrochemical modeling via meso-scale simulation: (a) Schematic illustration of the role of surface energy in governing the SEI morphology. Current distribution within the SEI and electrolyte for (b) higher ($h/t=1$) and (c) lower ($h/t=0.2$) morphological heterogeneities of the SEI structure, $i_{App}=1$ mA cm^{-2}. (d) Effect of current rate and SEI morphology on reaction heterogeneity, denoted as the ratio of maximum (i_{max}) and minimum (i_{min}) reaction current density at the interface. (e) Reaction current distribution at the electrode interface for different values of SEI conductivity. (f) Effect of SEI conductivity and morphology on reaction heterogeneity.

between the maximum and the minimum thickness of the SEI and t is the maximum thickness. A higher value of h/t denotes a larger morphological heterogeneity of the SEI. Figure 7(b) illustrates how morphological heterogeneity ($h/t=1$) of the SEI leads to non-uniform ionic transport, resulting in reaction current focusing in regions of lower SEI thickness. The SEI-driven transport heterogeneities subsequently lead to non-uniform Na deposition at the electrode interface. On the other hand, a more uniform SEI morphology ($h/t=0.2$) results in homogeneous current distributions near the interface as observed in Figure 7(c). The effect of current rate and SEI morphology on reaction heterogeneity is examined in Figure 7(d). Here, the reaction heterogeneity is denoted as the ratio of maximum and minimum reaction current densities at the interface, i.e., i_{max}/i_{min}. While the electrodeposition instability increases at higher current densities, this effect exacerbates for a higher heterogeneity in SEI morphology as observed in Figure 7(d), which explains the compact Na deposition at Te–Cu electrode and larger range of Na deposit thicknesses at Cu electrode for different current rates.

As discussed in the previous section, the SEI composition depends on the substrate and NaF is found to be a major SEI component for Te–Cu electrode while the SEI on Cu electrode contains relatively more NaH/NaOH. Alkali metal fluorides have been found to have high ionic conductivities at metal interfaces and form a more uniform and compact SEI.[34] To investigate the effect of SEI ionic conductivity, Figure 7(e) shows the reaction current profiles for different values of the nondimensional parameter, $K = k_{SEI}/k_{Elec}$, where k_{SEI} and k_{Elec} are the ionic conductivities of the SEI and electrolyte, respectively. The reaction non-uniformity is lower for a more conductive SEI and hence a more stable Na morphology is observed for Te–Cu electrode consisting of NaF-rich SEI layers. Figure 7(f) shows the combined effect of SEI conductivity and SEI structure on the reaction heterogeneity descriptor, i_{max}/i_{min}. The enhanced wetting and higher ionic conductivity of SEI components make Na deposition on Te–Cu electrode more stable than deposition on Cu electrode.

Conclusions

In summary, we investigate the role of current collector wettability on cycle-one microstructure of electrodeposited sodium metal and its solid electrolyte interphase (SEI). Experiments demonstrate complex support and rate dependent interrelations, which are further analyzed with modeling to predict their effect on localized current density, and onset of electrochemical instability to form geometrical perturbations that become dendrites with cycling.

Acknowledgements

We gratefully acknowledge support from the U.S. Department of Energy, Office of Science, Basic Energy Sciences under Award# DE-SC0023260. This research used resources, Full Field X-ray Imaging (FXI) beamline (18-ID), Complex Materials Scattering (CMS) beamline (11-BM), and Quick X-ray Absorption and Scattering (QAS) beamline (7-BM) of the National Synchrotron Light Source II, a U.S. Department of Energy (DOE) Office of Science by Brookhaven National Laboratory under Contract No. DE-SC0012704. This research used scanning electron microscopy capabilities of the Center for Functional Nanomaterials (CFN), which is a U.S. DOE Office of Science Facility, at Brookhaven National Laboratory under Contract No. DE-SC0012704. Cryo-EM was performed at the Center for Integrated Nanotechnologies, an Office of Science User Facility operated for the U.S. Department of Energy (DOE) Office of Science. The Los Alamos National Laboratory, an affirmative action equal opportunity employer, is managed by Triad National Security, LLC for the U.S. Department of Energy's NNSA, under contract 89233218CNA000001. This work was supported by The Welch Foundation (F-2206).

Conflict of Interest

The authors declare no conflict of interest.

Data Availability Statement

The data that support the findings of this study are available from the corresponding author upon reasonable request.

Keywords: sodium metal battery · sodium metal anode · solid electrolyte interphase (SEI) · fiber texture · film growth

[1] a) Y. Sun, J.-C. Li, H. Zhou, S. Guo, *Energy Environ. Sci.* **2023**, *16*, 4759; b) J.-M. Tarascon, *Joule* **2020**, *4*, 1616; c) J. Xiao, N. Xiao, K. Li, L. Zhang, X. Ma, Y. Li, C. Leng, J. Qiu, *Adv. Funct. Mater.* **2022**, *32*, 2111133; d) H. Yang, F. He, M. Li, F. Huang, Z. Chen, P. Shi, F. Liu, Y. Jiang, L. He, M. Gu, *Adv. Mater.* **2021**, *33*, 2106353; e) R. Cao, K. Mishra, X. Li, J. Qian, M. H. Engelhard, M. E. Bowden, K. S. Han, K. T. Mueller, W. A. Henderson, J.-G. Zhang, *Nano Energy* **2016**, *30*, 825.

[2] a) X.-B. Cheng, R. Zhang, C.-Z. Zhao, Q. Zhang, *Chem. Rev.* **2017**, *117*, 10403; b) B. S. Vishnugopi, F. Hao, A. Verma, P. P. Mukherjee, *ACS Appl. Mater. Interfaces* **2020**, *12*, 23931; c) B. S. Vishnugopi, F. Hao, A. Verma, P. P. Mukherjee, *Phys. Chem. Chem. Phys.* **2020**, *22*, 11286; d) G. G. Eshetu, G. A. Elia, M. Armand, M. Forsyth, S. Komaba, T. Rojo, S. Passerini, *Adv. Energy Mater.* **2020**, *10*, 2000093; e) W. Liu, P. Li, W. Wang, D. Zhu, Y. Chen, S. Pen, E. Paek, D. Mitlin, *ACS Nano* **2018**, *12*, 12255; f) P. Bai, J. Li, F. R. Brushett, M. Z. Bazant, *Energy Environ. Sci.* **2016**, *9*, 3221.

[3] a) Y. Wang, H. Dong, N. Katyal, B. S. Vishnugopi, M. K. Singh, H. Hao, Y. Liu, P. Liu, P. P. Mukherjee, G. Henkelman, *Adv. Energy Mater.* **2023**, 2204402; b) Y. Wang, H. Dong, N. Katyal, B. S. Vishnugopi, M. K. Singh, H. Hao, Y. Liu, P. Liu, P. P. Mukherjee, G. Henkelman, J. Watt, D. Mitlin, *Adv. Energy Mater.* **2023**, 13; c) Z. Lu, H. Yang, Q. H. Yang, P. He, H. Zhou, *Angew. Chem. Int. Ed.* **2022**, *61*, e202200410.

[4] a) L. Ma, J. Cui, S. Yao, X. Liu, Y. Luo, X. Shen, J.-K. Kim, *Energy Storage Mater.* **2020**, *27*, 522; b) L. Hu, J. Deng, Q. Liang, J. Wu, B. Ge, Q. Liu, G. Chen, X. Yu, *EcoMat* **2023**, *5*,

e12269; c) B. Thirumalraj, T. T. Hagos, C.-J. Huang, M. A. Teshager, J.-H. Cheng, W.-N. Su, B.-J. Hwang, *J. Am. Chem. Soc.* **2019**, *141*, 18612; d) B. Sun, P. Li, J. Zhang, D. Wang, P. Munroe, C. Wang, P. H. L. Notten, G. Wang, *Adv. Mater.* **2018**, DOI: 10.1002/adma.2018013341801334; e) Y. Xu, C. Wang, E. Matios, J. Luo, X. Hu, Q. Yue, Y. Kang, W. Li, *Adv. Energy Mater.* **2020**, *10*, 2002308.

[5] a) X. Zheng, H. Fu, C. Hu, H. Xu, Y. Huang, J. Wen, H. Sun, W. Luo, Y. Huang, *J. Phys. Chem. Lett.* **2019**, *10*, 707; b) S. Wang, W. Cai, Z. Sun, F. Huang, Y. Jie, Y. Liu, Y. Chen, B. Peng, R. Cao, G. Zhang, S. Jiao, *Chem. Commun.* **2019**, *55*, 14375; c) X. Zheng, Z. Gu, X. Liu, Z. Wang, J. Wen, X. Wu, W. Luo, Y. Huang, *Energy Environ. Sci.* **2020**, *13*, 1788; d) X. Hu, E. Matios, Y. Zhang, C. Wang, J. Luo, W. Li, *Angew. Chem. Int. Ed.* **2021**, *60*, 5978; e) J. Luo, Y. Zhang, E. Matios, P. Wang, C. Wang, Y. Xu, X. Hu, H. Wang, B. Li, W. Li, *Nano Lett.* **2022**, *22*, 1382.

[6] a) Z. Tu, S. Choudhury, M. J. Zachman, S. Wei, K. Zhang, L. F. Kourkoutis, L. A. Archer, *Nat. Energy* **2018**, *3*, 310; b) L. Zhang, X. Zhu, G. Wang, G. Xu, M. Wu, H. K. Liu, S. X. Dou, C. Wu, *Small* **2021**, *17*, 2007578; c) M. Zhu, G. Wang, X. Liu, B. Guo, G. Xu, Z. Huang, M. Wu, H. K. Liu, S. X. Dou, C. Wu, *Angew. Chem. Int. Ed.* **2020**, *59*, 6596; d) P. Liu, L. Miao, Z. Sun, X. Chen, Y. Si, Q. Wang, L. Jiao, *Angew. Chem. Int. Ed.* **2023**, *62*, e202312413; e) S. Wang, Y. Chen, Y. Jie, S. Lang, J. Song, Z. Lei, S. Wang, X. Ren, D. Wang, X. Li, R. Cao, G. Zhang, S. Jiao, *Small Methods* **2020**, 4.

[7] a) F. Wu, J. Zhou, R. Luo, Y. Huang, Y. Mei, M. Xie, R. Chen, *Energy Storage Mater.* **2019**, *22*, 376; b) Y. Zhao, X. Yang, L. Y. Kuo, P. Kaghazchi, Q. Sun, J. Liang, B. Wang, A. Lushington, R. Li, H. Zhang, X. Sun, *Small* **2018**, *14*, 1703717; c) T. Li, J. Sun, S. Gao, B. Xiao, J. Cheng, Y. Zhou, X. Sun, F. Jiang, Z. Yan, S. Xiong, *Adv. Energy Mater.* **2020**, *11*, 2003699; d) X. He, S. Jin, L. Miao, Y. Cai, Y. Hou, H. Li, K. Zhang, Z. Yan, J. Chen, *Angew. Chem. Int. Ed.* **2020**, *59*, 16705.

[8] a) Q. Li, Z. Zhang, S. Dong, C. Li, X. Ge, Z. Li, J. Ma, L. Yin, *Part. Part. Syst. Charact.* **2017**, *34*, 1600115; b) S. Tang, Y. Y. Zhang, X. G. Zhang, J. T. Li, X. Y. Wang, J. W. Yan, D. Y. Wu, M. S. Zheng, Q. F. Dong, B. W. Mao, *Adv. Mater.* **2019**, *31*, 1807495; c) Y. Deng, J. Zheng, Q. Zhao, J. Yin, P. Biswal, Y. Hibi, S. Jin, L. A. Archer, *Small* **2022**, *18*, 2203409; d) W. Wu, S. Hou, C. Zhang, L. Zhang, *ACS Appl. Mater. Interfaces* **2020**, *12*, 27300.

[9] Y. Wang, H. Dong, N. Katyal, H. Hao, P. Liu, H. Celio, G. Henkelman, J. Watt, D. Mitlin, *Adv. Mater.* **2022**, *34*, e2106005.

[10] a) Y. Li, Y. Li, A. Pei, K. Yan, Y. Sun, C.-L. Wu, L.-M. Joubert, R. Chin, A. L. Koh, Y. Yu, *Science* **2017**, *358*, 506; b) X. Wang, M. Zhang, J. Alvarado, S. Wang, M. Sina, B. Lu, J. Bouwer, W. Xu, J. Xiao, J.-G. Zhang, *Nano Lett.* **2017**, *17*, 7606; c) X. Wang, Y. Li, Y. S. Meng, *Joule* **2018**, *2*, 2225; d) B. Han, Y. Zou, Z. Zhang, X. Yang, X. Shi, H. Meng, H. Wang, K. Xu, Y. Deng, M. Gu, *Nat. Commun.* **2021**, *12*, 3066.

[11] a) M. I. Nandasiri, L. E. Camacho-Forero, A. M. Schwarz, V. Shutthanandan, S. Thevuthasan, P. B. Balbuena, K. T. Mueller, V. Murugesan, *Chem. Mater.* **2017**, *29*, 4728; b) K. N. Wood, K. X. Steirer, S. E. Hafner, C. Ban, S. Santhanagopalan, S.-H. Lee, G. Teeter, *Nat. Commun.* **2018**, *9*, 2490.

[12] a) C. Wan, S. Xu, M. Y. Hu, R. Cao, J. Qian, Z. Qin, J. Liu, K. T. Mueller, J.-G. Zhang, J. Z. Hu, *ACS Appl. Mater. Interfaces* **2017**, *9*, 14741; b) L. Wang, A. Menakath, F. Han, Y. Wang, P. Y. Zavalij, K. J. Gaskell, O. Borodin, D. Iuga, S. P. Brown, C. Wang, *Nat. Chem.* **2019**, *11*, 789; c) A. J. Ilott, M. Mohammadi, H. J. Chang, C. P. Grey, A. Jerschow, *Proc. Nat. Acad. Sci.* **2016**, *113*, 10779.

[13] Z. Shadike, H. Lee, O. Borodin, X. Cao, X. Fan, X. Wang, R. Lin, S.-M. Bak, S. Ghose, K. Xu, *Nat. Nanotechnol.* **2021**, *16*, 549.

[14] Y. Ji, J. Qiu, W. Zhao, T. Liu, Z. Dong, K. Yang, G. Zheng, G. Qian, M. Yang, Q. Chen, *Chem* **2023**, *9*, 2943.

[15] a) C.-A. Lo, C.-C. Chang, Y.-W. Tsai, S.-K. Jiang, B. J. Hwang, C.-Y. Mou, H.-L. Wu, *ACS Appl. Energ. Mater.* **2021**, *4*, 5132; b) R. M. Kasse, N. R. Geise, J. S. Ko, J. N. Weker, H.-G. Steinrück, M. F. Toney, *J. Mater. Chem. A* **2020**, *8*, 16960; c) N. R. Geise, R. M. Kasse, J. Nelson Weker, H.-G. Steinrück, M. F. Toney, *Chem. Mater.* **2021**, *33*, 7537; d) O. O. Taiwo, D. P. Finegan, J. Paz-Garcia, D. S. Eastwood, A. Bodey, C. Rau, S. Hall, D. J. Brett, P. D. Lee, P. R. Shearing, *Phys. Chem. Chem. Phys.* **2017**, *19*, 22111.

[16] a) H. Jung, B. Lee, M. Lengyel, R. Axelbaum, J. Yoo, Y. S. Kim, Y.-S. Jun, *J. Mater. Chem. A* **2018**, *6*, 4629; b) J. Seok, J.-H. Hyun, A. Jin, J. H. Um, H. D. Abruña, S.-H. Yu, *ACS Appl. Mater. Interfaces* **2022**, *14*, 10438; c) R. Haas, C. Pompe, M. Osenberg, A. Hilger, I. Manke, B. Mogwitz, U. Maitra, D. Langsdorf, D. Schröder, *Energy Technol.* **2019**, *7*, 1801146.

[17] Y. Wang, Y. Liu, M. Nguyen, J. Cho, N. Katyal, B. S. Vishnugopi, H. Hao, R. Fang, N. Wu, P. Liu, *Adv. Mater.* **2023**, *35*, 2206762.

[18] a) C. Bao, B. Wang, P. Liu, H. Wu, Y. Zhou, D. Wang, H. Liu, S. Dou, *Adv. Funct. Mater.* **2020**, *30*, 2004891; b) Y. Li, F. Wu, Y. Li, M. Liu, X. Feng, Y. Bai, C. Wu, *Chem. Soc. Rev.* **2022**, *51*, 4484.

[19] a) L. Chen, R. Yan, M. Oschatz, L. Jiang, M. Antonietti, K. Xiao, *Angew. Chem. Int. Ed. Engl.* **2020**, *59*, 9067; b) E. Herrero, L. J. Buller, H. D. Abruña, *Chem. Rev.* **2001**, *101*, 1897.

[20] M. Ge, D. S. Coburn, E. Nazaretski, W. Xu, K. Gofron, H. Xu, Z. Yin, W.-K. Lee, *Appl. Phys. Lett.* **2018**, 113.

[21] U. Dahmen, *Acta Metall.* **1982**, *30*, 63.

[22] H. Hao, Y. Liu, S. M. Greene, G. Yang, K. G. Naik, B. S. Vishnugopi, Y. Wang, H. Celio, A. Dolocan, W.-Y. Tsai, R. Fang, J. Watt, P. P. Mukherjee, D. J. Siegel, D. Mitlin, **2023**, *13*, 2301338.

[23] a) X. Hu, Y. Gao, B. Zhang, L. Shi, Q. Li, *EcoMat* **2022**, 4; b) L. Shi, A. Xu, T. Zhao, *ACS Appl. Mater. Interfaces* **2017**, *9*, 1987.

[24] a) C. Ophus, E. Luber, D. Mitlin, *Acta Mater.* **2009**, *57*, 1327; b) P. Smereka, X. Li, G. Russo, D. J. Srolovitz, *Acta Mater.* **2005**, *53*, 1191; c) D. Srolovitz, C. Battaile, X. Li, J. Butler, *Acta Mater.* **1999**, *47*, 2269; d) A. Van der Drift, *Philips Res. Rep.* **1967**, *22*, 267.

[25] a) G. Vetterick, J. Baldwin, A. Misra, M. Taheri, *J. Appl. Phys.* **2014**, 116; b) C. Wild, N. Herres, P. Koidl, *J. Appl. Phys.* **1990**, *68*, 973.

[26] a) D. T. Boyle, Y. Li, A. Pei, R. A. Vila, Z. Zhang, P. Sayavong, M. S. Kim, W. Huang, H. Wang, Y. Liu, R. Xu, R. Sinclair, J. Qin, Z. Bao, Y. Cui, *Nano Lett.* **2022**, *22*, 8224; b) X. Yuan, B. Liu, M. Mecklenburg, Y. Li, *Nature* **2023**, *620*, 86.

[27] F. Shi, A. Pei, A. Vailionis, J. Xie, B. Liu, J. Zhao, Y. Gong, Y. Cui, *Proc. Natl. Acad. Sci. USA* **2017**, *114*, 12138.

[28] a) W. Liu, Z. Chen, Z. Zhang, P. Jiang, Y. Chen, E. Paek, Y. Wang, D. Mitlin, *Energy Environ. Sci.* **2021**, *14*, 382; b) W. Liu, P. Liu, D. Mitlin, *Adv. Energy Mater.* **2020**, 10; c) B. Lee, E. Paek, D. Mitlin, S. W. Lee, *Chem. Rev.* **2019**, *119*, 5416.

[29] a) B. Sayahpour, W. Li, S. Bai, B. Lu, B. Han, Y.-T. Chen, G. Deysher, S. Parab, P. Ridley, G. Raghavendran, L. H. B. Nguyen, M. Zhang, Y. S. Meng, *Energy Environ. Sci.* **2024**, *17*, 1216; b) B. Han, Y. Zou, Z. Zhang, X. Yang, X. Shi, H. Meng, H. Wang, K. Xu, Y. Deng, M. Gu, *Nat. Commun.* **2021**, *12*, 3066.

[30] Z. Xu, J. Yang, T. Zhang, L. Sun, Y. Nuli, J. Wang, S. Hirano, *Adv. Funct. Mater.* **2019**, *29*, 1901924.

[31] A. Jain, S. P. Ong, G. Hautier, W. Chen, W. D. Richards, S. Dacek, S. Cholia, D. Gunter, D. Skinner, G. Ceder, *APL materials* **2013**, 1.

[32] a) R. A. Vilá, D. T. Boyle, A. Dai, W. Zhang, P. Sayavong, Y. Ye, Y. Yang, J. A. Dionne, Y. Cui, *Sci. Adv.* **2023**, *9*, eadf3609; b) S. Tan, J.-M. Kim, A. Corrao, S. Ghose, H. Zhong, N. Rui, X. Wang, S. Senanayake, B. J. Polzin, P. Khalifah, *Nat. Nanotechnol.* **2023**, *18*, 243.

[33] a) C. Gong, S. D. Pu, S. Zhang, Y. Yuan, Z. Ning, S. Yang, X. Gao, C. Chau, Z. Li, J. Liu, *Energy Environ. Sci.* **2023**, *16*, 535; b) Y. Xiang, G. Zheng, Z. Liang, Y. Jin, X. Liu, S. Chen, K. Zhou, J. Zhu, M. Lin, H. He, *Nat. Nanotechnol.* **2020**, *15*, 883.

[34] a) C. Gong, S. D. Pu, X. Gao, S. Yang, J. Liu, Z. Ning, G. J. Rees, I. Capone, L. Pi, B. Liu, *Adv. Energy Mater.* **2021**, *11*, 2003118; b) R. Guo, B. M. Gallant, *Chem. Mater.* **2020**, *32*, 5525; c) Z. W. Seh, J. Sun, Y. Sun, Y. Cui, *ACS Cent. Sci.* **2015**, *1*, 449.

Manuscript received: July 3, 2024
Accepted manuscript online: September 15, 2024
Version of record online: ■■, ■■

Forschungsartikel

Batteries

C.-A. Lo, Y. Wang, V. R. Kankanallu, A. Singla, D. Yen, X. Zheng, K. G. Naik, B. S. Vishnugopi, C. Campbell, V. Raj, C. Zhao, L. Ma, J. Bai, F. Yang, R. Li, M. Ge, J. Watt, P. P. Mukherjee, D. Mitlin,* Y.-c. Karen Chen-Wiegart* ____ **e202412550**

Interdependence of Support Wettability - Electrodeposition Rate- Sodium Metal Anode and SEI Microstructure

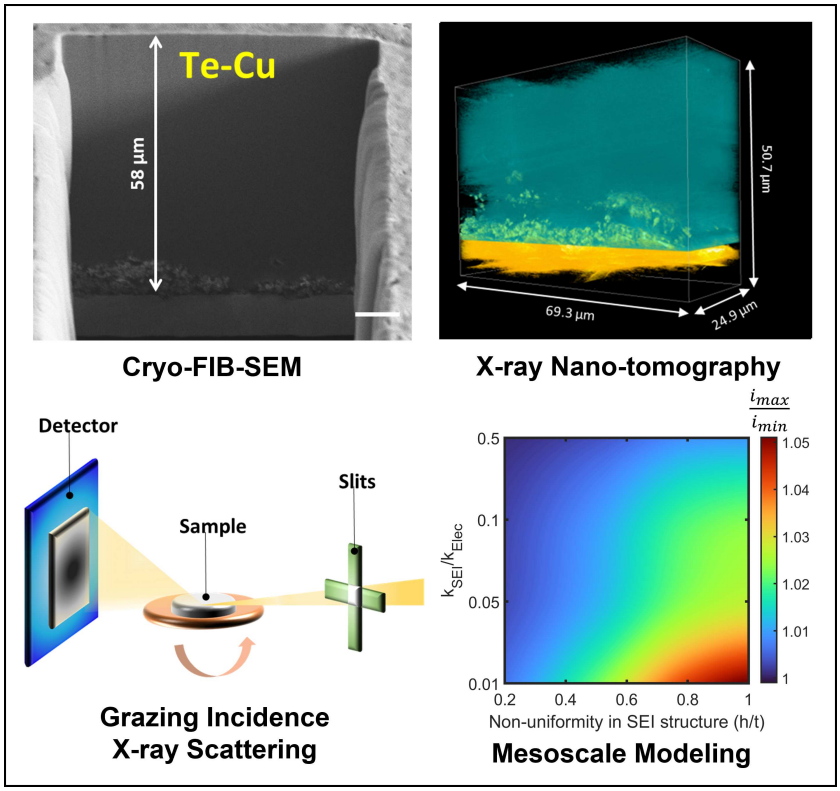

This study examines how current collector chemistry and electrodeposition rate affect microstructure of sodium metal and its solid electrolyte interphase. Synchrotron X-ray nanotomography, grazing-incidence wide-angle X-ray scattering, and cryogenic focused ion beam microscopy reveal differences in film morphology, internal porosity, and crystallographic preferred orientation. Mesoscale modeling delineates the role of SEI on electrodeposit growth and onset of electrochemical instability.